



Cite this: *Phys. Chem. Chem. Phys.*,
2019, 21, 24406

A global CHIPR potential energy surface for ground-state C₃H and exploratory dynamics studies of reaction C₂ + CH → C₃ + H[†]

C. M. R. Rocha ^a and A. J. C. Varandas *^{ab}

A full-dimensional global potential-energy surface (PES) is first reported for ground-state doublet C₃H using the combined-hyperbolic-inverse-power-representation (CHIPR) method and accurate *ab initio* energies extrapolated to the complete basis set limit. The PES is based on a many-body expansion-type development where the two-body and three-body energy terms are from our previously reported analytic potentials for C₂H(²A') and C₃(¹A', ³A'), while the effective four-body one is calibrated using an extension of the CHIPR formalism for tetratomics. The final form is shown to accurately reproduce all known stationary structures of the PES, some of which are unreported thus far, and their interconversion pathways. Moreover, it warrants by built-in construction the appropriate permutational symmetry and describes in a physically reasonable manner all long-range features and the correct asymptotic behavior at dissociation. Exploratory quasi-classical trajectory calculations for the reaction C₂ + CH → C₃ + H are also performed, yielding thermalized rate coefficients for temperatures up to 4000 K.

Received 3rd September 2019,
Accepted 17th October 2019

DOI: 10.1039/c9cp04890a

rsc.li/pccp

1 Introduction

Small carbon-bearing species C_n and C_nH (*n* = 1–3) are ubiquitous in the interstellar medium (ISM).¹ They are particularly conspicuous and known to drive the C-chemistry² in cold dense clouds^{3–5} and in circumstellar envelopes of evolved C-rich stars.^{6–8} In these former environments, the radical⁹ C₃H – whose potential energy surface¹⁰ (PES) entails all the above smaller species as fragments – plays a prominent role, reaching relatively high fractional abundances ($\approx 10^{-9}$) when compared to H₂.^{2,11} In molecular cloud cores, both its cyclic¹² (c-C₃H; cyclopropynylidene) and linear¹³ (ℓ-C₃H; propynylidene) isomers are thought to be formed *via* dissociative electron recombination of¹⁴ c,ℓ-C₃H₂⁺/C₃H₃⁺ or through the atom-neutral pathway^{14–17} C + C₂H₂, the latter being an important prototypical reaction implied in the growth of C-chains in space.^{15–17} This has motivated further surmises¹⁸ on the role of c-C₃H as a key intermediate (*via* c-C₃H₂ formation) in the synthesis of interstellar polycyclic aromatic hydrocarbon molecules – widely recognized as potential carriers of the so-called unidentified infrared bands.¹⁹

The prevalence of C₃H in the ISM and its relevance to C-chain formation have stimulated considerable experimental^{12,20–28} and theoretical^{29–42} efforts toward understanding its intricate chemistry.

Yet, most of these studies have thus far mainly concerned the determination of relative energetics, symmetry and spectra of its isomeric forms.

ℓ-C₃H has a ²Π electronic ground-state and its two bending modes, ν_4 (C–C–H) and ν_5 (C–C–C), are perturbed by Renner–Teller (RT) and spin–orbit effects.¹³ The first laboratory detection of ℓ-C₃H was reported by Gottlieb *et al.*²⁰ who measured its microwave spectra in both ²Π_{1/2} and ²Π_{3/2} (ground) vibronic states. Subsequently, Yamamoto²¹ and Kanada *et al.*²² recorded pure rotational lines in ν_4 (²Σ^μ) and found that ℓ-C₃H has an extremely low vibrationally excited state (≈ 27 cm⁻¹ above ²Π_{1/2}) which is caused by the strong RT effect in the ν_4 bending mode,²¹ its molecular structure was first derived from the rotational spectral data.²² Subsequent studies were mainly devoted to improving previously reported spectroscopic constants for the ²Π_r and ν_4 (²Σ^μ) states²³ and extending the range of rotational transitions within the ²Σ vibrationally excited manifold;²⁴ to our knowledge, no definitive assignment of the ν_5 (²Σ^μ) fundamental has yet been made. Infrared (IR) vibrational band centers for the stretching modes (ν_1 , ν_2 and ν_3) were provided by Jiang *et al.*²⁵ in the Ar matrix, and by Sheehan *et al.*²⁶ in the gas phase.

c-C₃H has a ²B₂¹² ground electronic state and was first detected in the laboratory by Yamamoto *et al.*^{12,27} *via* microwave spectroscopy. Based on the predicted rotational constants, the authors reported the molecular structure of c-C₃H, confirming its C_{2v} nature.²⁷ Moreover, using inertial defect considerations, they estimated the C–C asymmetric mode (ν_4 ; which lowers the symmetry from C_{2v} to C_s) to be fairly low (≈ 508 cm⁻¹) and

^a Department of Chemistry and Coimbra Chemistry Centre, University of Coimbra, 3004-535 Coimbra, Portugal. E-mail: cmrocha@quimica.uc.pt, varandas@uc.pt

^b School of Physics and Physical Engineering, Qufu Normal University, 273165, P. R. China

† Electronic supplementary information (ESI) available. See DOI: 10.1039/c9cp04890a

attributed it to the vibronic interactions [*i.e.*, pseudo Jahn–Teller (PJT) effects³⁶] between the ground ${}^2\text{B}_2$ and first ${}^2\text{A}_1$ excited states.²⁷ In turn, Sheehan *et al.*²⁶ reported gas-phase estimates of the ν_2 (ring stretching) and ν_3 (scissoring) fundamentals of $c\text{-C}_3\text{H}$; apart from such rough estimates, no accurate experimental IR band centers are available for this form³⁹ thus far.

Early *ab initio* calculations^{12,22,25,29–34} on C_3H were primarily devoted to elucidate discrepancies between the predicted symmetries of the linear and cyclic forms and the ones actually inferred from microwave spectroscopy^{22,27} (energetically, the best estimate³⁴ places $c\text{-C}_3\text{H} \approx 14 \text{ kJ mol}^{-1}$ more stable than $\ell\text{-C}_3\text{H}$). From these studies, a general trend can be stated: depending on the electronic structure method (single-reference *versus* truncated-space multireference) and the utilized basis set (size), the $c\text{-C}_3\text{H}$ ($\ell\text{-C}_3\text{H}$) C_{2v} ($C_{\infty v}$) structure might be in a transition state and that a slightly distorted C_s form might be preferred. For the cyclic isomer, such a symmetry breaking issue was first dealt with by Stanton and coworkers.^{36,37} Using the equation-of-motion coupled cluster method in the single and double approximations for ionized states (EOMIP-CCSD), they first emphasized the role of the basis set effect to the accurate determination of its C_{2v} symmetry and to the increase of the $\text{X}^2\text{B}_2 \rightarrow \text{A}^2\text{A}_1$ excitation energy. As noted by them, the PJT effect between such states – which had previously been considered²⁷ as the cause of the possible C_s equilibrium structure – is weakened when the size of the one-electron basis set is increased. Similar conclusions (regarding the N -electron basis) were subsequently drawn by Halvick³⁸ at the multireference configuration interaction level of theory [MRCI+Q] with cc-pVXZ ($X = D, T, Q$) basis sets;^{43,44} he has shown that the PES along the C–C asymmetric w_4 mode becomes increasingly stiff with correlation energy. Recently, Bassett and Fortenberry³⁹ reported a quartic force field (QFF) for $c\text{-C}_3\text{H}$ from a composite scheme – based on accurate energies extrapolated to the complete-basis-set (CBS) limit at the CCSD(T)/aug-cc-pVXZ level of theory [briefly CCSD(T)/AVXZ] from basis-set cardinal numbers $X = T, Q, 5$, then additively corrected for core correlation and scalar relativistic³⁹ effects. From the QFF so obtained and using second-order vibrational perturbation theory (VPT2),³⁹ the authors reported rotational constants, structural parameters and anharmonic vibrational frequencies for the X^2B_2 ground-state; to our knowledge, these are the best *ab initio* estimates so far. The spectroscopic characterization of the C_3H isomers has also been done recently by Bennedjai *et al.*⁴⁰ at the explicitly correlated CCSD(T) level of theory, CCSD(T)-F12/AVTZ. Note that, for the linear form, the most comprehensive theoretical study to date was carried out by Perić *et al.*⁴¹ who provided local MRCI+Q/cc-pVTZ PESs (including relativistic effects) for both ${}^2\text{A}'$ and ${}^2\text{A}''$ electronic states correlating with the ${}^2\Pi$ term. These PESs were subsequently used to compute the vibronic and spin-orbit structure of the $\ell\text{-C}_3\text{H}$ spectrum using a variational approach.⁴¹ In their work, the authors highlight the extremely flat nature of the CCC-H bending potential curve (${}^2\text{A}'$) and, like others,^{22,32} do not rule out the possibility of its quasilinearity based on the limited accuracy of their PESs. Despite this and the fact that their local forms assume $C_{\infty v}$ equilibrium geometries, the values of the various spectroscopic parameters have shown

excellent agreement with the experimental results. In fact, as shown by Ding *et al.*²⁸ at both the complete active space self-consistent field (CASSCF) and the CCSD(T) level of theory, the minimum structure of $\ell\text{-C}_3\text{H}$ tends to change from a bent to a linear geometry with basis set size enhancement (from AVTZ to AVQZ). In turn, Mebel and Kaiser⁴² reported an *ab initio* study of the ground-state C_3H PES. Using CCSD(T)/6-311+G(3df,2p), they first noted that the linear and cyclic forms rearrange to each other *via* a ring opening step through an asymmetric transition state (hereafter denoted as $\ell\text{-C}_3\text{H}$) with a barrier of about 115 kJ mol^{-1} . Moreover, they remarked that, besides $\text{C}({}^3\text{P}_J) + \text{C}_2\text{H}_2(\text{X}^1\Sigma_g^+)$, the (barrierless) reactions of $\text{CH}(\text{X}^2\Pi) + \text{C}_2(\text{X}^1\Sigma_g^+)$ and $\text{C}({}^3\text{P}) + \text{C}_2\text{H}(\text{X}^2\Sigma^+)$ represent facile neutral-neutral (exothermic) pathways yielding a carbon trimer in cold interstellar environments.

All the above features make C_3H a unique and challenging species from both chemical and astrophysical viewpoints. Certainly, the implications related to its spectroscopy and reaction dynamics in all those fields highlight the need for a global PES for the title system. The major goal of this work is therefore to provide such a form for the ground-state doublet C_3H that correlates with the ${}^2\Pi$ state at linear geometries, with ${}^2\text{B}_2$ at cyclic ones and to the correct fragmentation channels. For this purpose, accurate CBS extrapolated *ab initio* energies are employed and modeled analytically using the combined-hyperbolic-inverse-power-representation (CHIPR) method.^{45–47}

The paper is organized as follows. Section 2 provides an overview of the *ab initio* calculations and CBS extrapolations performed here. The details of the analytical modelling are described in Section 3, while the topographical features of the final PES are discussed in Section 4. Section 5 reports a preliminary quasi-classical trajectory study of the $\text{C}_2 + \text{CH}$ reaction, while Section 6 gathers the conclusions.

2 Ab initio calculations

All calculations have been performed at the spin-restricted open-shell RCCSD(T) [CC for brevity] level of theory^{48–50} using the ROHF determinant as reference.⁵¹ The AVXZ ($X = D, T$) basis sets of Dunning and co-workers^{43,44} were employed throughout, with the calculations done using MOLPRO.⁵² All *ab initio* energies have subsequently been CBS extrapolated. As usual,⁵³ extrapolations were done separately for the HF and correlation (cor) components⁵³

$$E_{\infty}^{\text{CBS}}(\mathbf{R}) = E_{\infty}^{\text{HF}}(\mathbf{R}) + E_{\infty}^{\text{COR}}(\mathbf{R}), \quad (1)$$

where E_{∞}^{CBS} is the total CBS energy and \mathbf{R} a six-dimensional coordinate vector.

For the HF energy, a two-point extrapolation protocol⁵⁴ has been utilized,

$$E_X^{\text{HF}}(\mathbf{R}) = E_{\infty}^{\text{HF}}(\mathbf{R}) + A e^{-\beta x}, \quad (2)$$

where $x = d(2.08)$, $t(2.96)$ are hierarchical numbers^{55,56} associated with $X = D, T$, $\beta = 1.62$, and A is a parameter to be calibrated from ROHF/AVXZ energies.⁵⁴ In turn, the extrapolated core contributions

are obtained *via* the uniform singlet- and triplet-pair extrapolation (USTE) protocol^{55,57–59}

$$E_X^{\text{cor}}(\mathbf{R}) = E_{\infty}^{\text{cor}}(\mathbf{R}) + \frac{A_3}{x^3}, \quad (3)$$

where $d(1.91)$ and $t(2.71)$ are CC-type x numbers,⁵⁵ with A_3 calibrated from the raw CC core energies.

With the above CC/CBS(d,t) protocol, a total of 42 538 symmetry unrelated grid points have been selected to map all relevant regions of the 6D nuclear configuration space while ensuring a balanced global representation of the PES; to assess all geometrical structures and coordinate systems considered here, see Fig. S1 of the ESI.†

3 CHIPR PES

Within the CHIPR framework,^{45,46} the ground-state doublet PES of C₃H assumes the following many-body expansion (MBE)¹⁰ form

$$V(\mathbf{R}) = V^{(2+3)}(\mathbf{R}) + V^{(4)}(\mathbf{R}), \quad (4)$$

where $V^{(2+3)}(\mathbf{R})$ accounts for the sum of two- and three-body interactions, and $V^{(4)}(\mathbf{R})$ accounts for the four-body ones. $\mathbf{R} = \{R_1, R_2, R_3, R_4, R_5, R_6\}$ is the set of interatomic separations (Fig. 1), with energy zero set to the infinitely separated ground-state C and H atoms.

3.1 Two-body and three-body energy terms

Following ref. 60, $V^{(2+3)}(\mathbf{R})$ in eqn (4) is defined as the lowest PES arising from the diagonalization of the 2×2 pseudo-diabatic matrix

$$\mathcal{H}_e = \begin{pmatrix} \mathcal{V}_{11}^{(2+3)}(\mathbf{R}) & \varepsilon(\mathbf{R}) \\ \varepsilon(\mathbf{R}) & \mathcal{V}_{22}^{(2+3)}(\mathbf{R}) \end{pmatrix}, \quad (5)$$

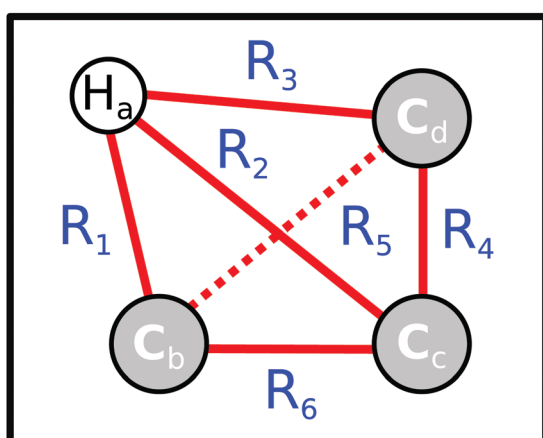


Fig. 1 Interparticle coordinate system employed in the construction of the CHIPR PES for ground-state C₃H; R_1 – R_3 define C–H bond distances, while R_4 – R_6 are C–C stretches.

Table 1 Energetics (in kJ mol⁻¹) of the various dissociation channels predicted from $V^{(2+3)}(\mathbf{R})$

Channel	Energy ^a		
	CC/CBS(d,t) ^b	$V^{(2+3)}$	Exp.
C ₂ (¹ S _g ⁺) + C(³ P) + H(² S)	-608.9	-620.3	-618.6 ± 2.1 ^c
C ₂ (³ P _u) + C(³ P) + H(² S)	-598.0	-612.0	-610.6 ± 2.1 ^c
CH(² Π) + 2C(³ P)	-355.1	-357.3	-351.2 ± 0.4 ^d
C ₂ (¹ S _g ⁺) + CH(² Π)	-963.9	-971.0	-969.8 ± 2.5 ^e
C ₂ (³ P _u) + CH(² Π)	-953.1	-963.3	-961.2 ± 2.5 ^e
ℓ -C ₃ (¹ S _g ⁺) + H(² S)	-1338.2	-1373.9	-1324.1 ± 13.0 ^c
c-C ₃ (³ A ₁) + H(² S)	-1255.5	-1279.5	
ℓ -C ₂ H(² Σ ⁺) + C(³ P)	-1108.5	-1107.3	-1110.7 ± 5.5 ^f

^a The units of energy are kJ mol⁻¹. Energies defined relative to the infinitely separated ground-state atoms. ^b CBS energies at CC/AVTZ optimized geometries. ^c Ref. 63. ^d Ref. 61. ^e Ref. 61 and 63. ^f Ref. 64.

where

$$\begin{aligned} \mathcal{V}_{11}^{(2+3)}(\mathbf{R}) = & \sum_{i=1}^3 V_{\text{CH}(^2\Pi)}^{(2)}(R_i) + \sum_{i=4}^6 V_{\text{C}_2(^3\Pi_u)}^{(2)}(R_i) \\ & + V_{\text{C}_2\text{H}(^2\text{A}')}^{(3)}(R_1, R_2, R_4) + V_{\text{C}_2\text{H}(^2\text{A}')}^{(3)}(R_1, R_3, R_5) \\ & + V_{\text{C}_2\text{H}(^2\text{A}')}^{(3)}(R_2, R_3, R_6) + V_{\text{C}_3(^1\text{A}')}^{(3)}(R_4, R_5, R_6) \end{aligned} \quad (6)$$

and

$$\begin{aligned} \mathcal{V}_{22}^{(2+3)}(\mathbf{R}) = & \sum_{i=1}^3 V_{\text{CH}(^2\Pi)}^{(2)}(R_i) + \sum_{i=4}^6 V_{\text{C}_2(^1\Sigma_g^+)}^{(2)}(R_i) \\ & + V_{\text{C}_2\text{H}(^2\text{A}')}^{(3)}(R_1, R_2, R_4) + V_{\text{C}_2\text{H}(^2\text{A}')}^{(3)}(R_1, R_3, R_5) \\ & + V_{\text{C}_2\text{H}(^2\text{A}')}^{(3)}(R_2, R_3, R_6) + V_{\text{C}_3(^3\text{A}')}^{(3)}(R_4, R_5, R_6) \end{aligned} \quad (7)$$

are diagonal terms constructed using previously reported two- and three-body (ground-state) potentials for C₂H(²A'),⁶¹ C₃(¹A')⁶² and C₃(³A')⁶⁰ (readers can refer to the original papers^{60–62} for details on the corresponding functional forms). In eqn (5), $\varepsilon(\mathbf{R})$ is a (small) coupling term chosen to warrant that the lowest eigenvalue of \mathcal{H}_e [eqn (5)] is continuous everywhere. The energetics of the various dissociation channels predicted from $V^{(2+3)}(\mathbf{R})$ are given in Table 1. Also shown for comparison are the corresponding values obtained from the CC/CBS(d,t) protocol as well as experimental estimates.^{61,63,64} As seen, the predicted thermochemistry of the $V^{(2+3)}(\mathbf{R})$'s fragments agrees quite well with the ones obtained from both theory and experiment. A somewhat larger discrepancy is observed for ℓ -C₃(¹S_g⁺) + H(²S), which can be attributed to the more attractive nature of the ℓ -C₃(¹S_g⁺)'s three-body term. Note that this dissociation channel is the one with the largest experimental uncertainty, while an accurate estimate of the C₃'s atomization energy still needs to be determined. Indeed, four-body energies vanish at these asymptotic channels, and hence play no role in the values reported in Table 1.

3.2 Four-body energy term

Once the $V^{(2+3)}(\mathbf{R})$ PES is obtained, the (effective) four-body term $\varepsilon^{(4)}(\mathbf{R})$ can then be expressed as

$$\varepsilon^{(4)}(\mathbf{R}) = E(\mathbf{R}) - V^{(2+3)}(\mathbf{R}), \quad (8)$$

where $E(\mathbf{R})$ is the CC/CBS(d,t) interaction energy (defined relative to the infinitely separated atoms) and $V^{(2+3)}(\mathbf{R})$ is the lowest characteristic value of eqn (5).

In CHIPR, $\varepsilon^{(4)}(\mathbf{R})$ [eqn (8)] can be conveniently modeled by^{45,46}

$$V^{(4)}(\mathbf{R}) = \sum_{i,j,k,l,m,n=0}^L C_{i,j,k,l,m,n} \left[\sum_{g \in G} \mathcal{P}_g^{(i,j,k,l,m,n)} (y_1^i y_2^j y_3^k y_4^l y_5^m y_6^n) \right], \quad (9)$$

where $C_{i,j,k,l,m,n}$ are expansion coefficients of a L th-degree polynomial ($i + j + k + l + m + n \leq L$) and y_p ($p = 1, 2, \dots, 6$) are transformed coordinates (see below). Note that, in the above equation, only those C 's that excite at least four modes and

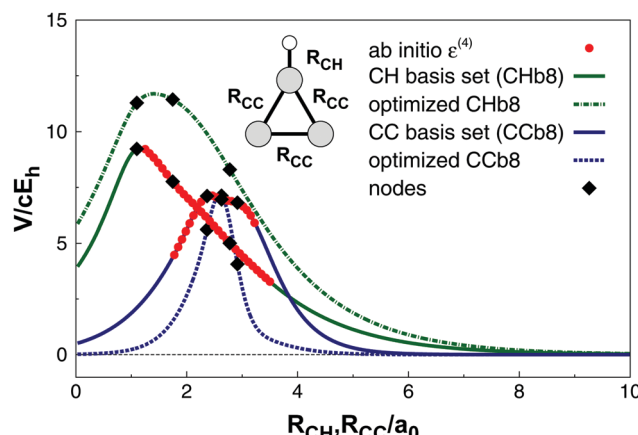


Fig. 2 C–H (y_1 – y_3) and C–C (y_4 – y_6) contracted basis sets of eqn (10) as determined from a fit to CC/CBS(d,t) four-body energies [$\varepsilon^{(4)}$ in eqn (8)]; see the text. The calibrating $c\text{-C}_3\text{H}$ reference geometry is made up of a D_{3h} structure of C_3 ($R_{\text{CC}} = 2.596a_0$) and the experimental²⁷ CH bond distance ($R_{\text{CH}} = 2.033a_0$). Solid diamonds indicate the origins ($R_{p,z}^{\text{ref}}$) of each primitive basis $\phi_{p,z}$ in eqn (10)–(13).

Table 2 Stratified root-mean-square deviations (in kJ mol^{-1}) of the final PES

Energy ^a	N^b	rmsd	\bar{T}_1^c	\bar{D}_1^c	\bar{T}_1/\bar{D}_1^c
50	1829	4.3	0.034	0.097	0.355
100	8100	5.6	0.036	0.098	0.363
150	14 680	7.1	0.036	0.098	0.364
200	19 699	7.6	0.035	0.098	0.363
300	24 859	7.6	0.035	0.097	0.364
400	29 052	7.8	0.035	0.096	0.368
500	30 820	8.0	0.035	0.096	0.369
1000	42 104	8.0	0.039	0.103	0.383
2000	42 483	8.0	0.039	0.103	0.382
3000	42 538	8.0	0.040	0.104	0.382

^a The units of energy are kJ mol^{-1} . Energy strata defined relative to the $c\text{-C}_3\text{H}$ global minimum with energy of $-0.6427E_h$. ^b Number of calculated points up to the indicated energy range. ^c Mean values of T_1 , D_1 and their ratio within each energy stratum. Values taken from CC/AVTZ calculations.

satisfy $i \leq j \leq k \leq l \leq m \leq n$ are included in the first summation. Following ref. 45 and 46, this former constraint is here specially devised so as to avoid any two- and three-body contributions. In eqn (9), the second summation runs over all permutation elements $g \in G$, where G is a subgroup of the S_4 symmetric group.⁶⁵ Thus, for an AB_3 -type molecule, $\mathcal{P}_g^{(i,j,k,l,m,n)}$ are the corresponding operators that reflect the action of the particle permutations [in cyclic notation⁶⁵] (), (3, 4), (2, 3), (2, 4), (2, 3, 4)

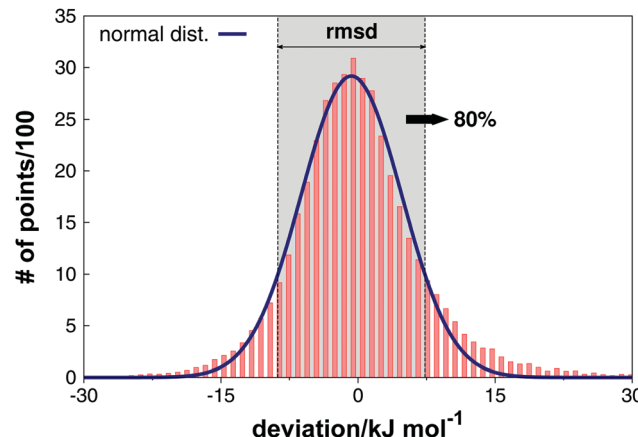


Fig. 3 Distribution of deviations between calculated and fitted *ab initio* points. The curve indicates a normal distribution adjusted to the data where 80% of the errors fall within the rmsd.

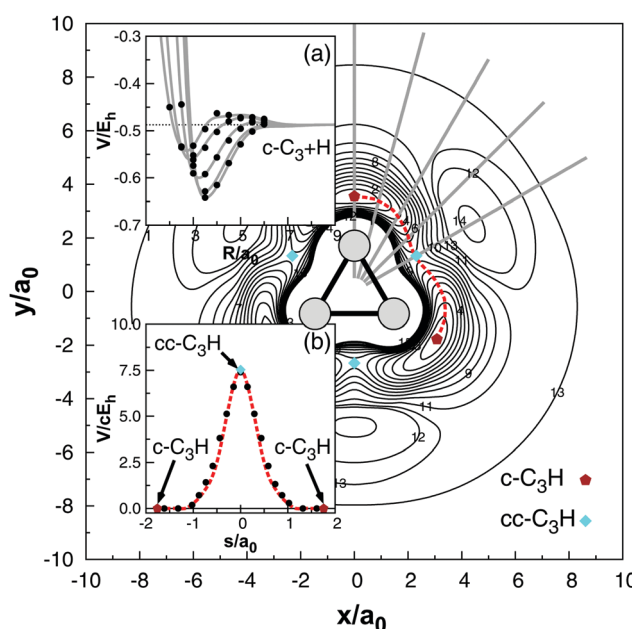


Fig. 4 Contour plot for an H atom moving around partially relaxed $c\text{-C}_3$ with center-of-mass fixed at the origin. Contours are equally spaced by 0.0135 E_h starting at $-0.65E_h$. The zero of energy is set relative to the infinitely separated atoms. The insets show (a) optimized 1D cuts and (b) minimum energy paths (where s is the reaction coordinate in mass-scaled a.u.) for the isomerization between symmetry equivalent $c\text{-C}_3\text{H}$ structures. In (b), the zero of energy corresponds to $c\text{-C}_3\text{H}$. Solid dots indicate *ab initio* CC/CBS(d,t) points while the dotted lines represent the dissociation energy limits predicted from $V^{(2+3)}(\mathbf{R})$.

and (2, 4, 3) onto the exponent set $\{i, j, k, l, m, n\}$ brought by the first summation of eqn (9). These actions generate therefore the

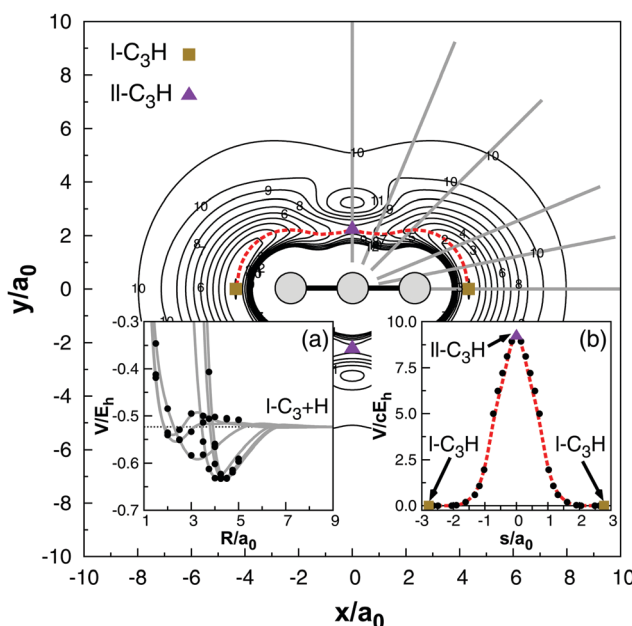


Fig. 5 Contour plot for an H atom moving around partially relaxed $\text{\texteta-}C_3$ which lies along the x axis with the central C atom at the origin. Contours are equally spaced by $0.0135E_h$ starting at $-0.65E_h$. The zero of energy is set relative to the infinitely separated atoms. The insets show (a) optimized 1D cuts and (b) minimum energy paths (where s is the reaction coordinate in mass-scaled a.u.) for the isomerization between symmetry equivalent $\text{\texteta-}C_3\text{H}$ structures. In (b), the zero of energy corresponds to $\text{\texteta-}C_3\text{H}$. Solid dots indicate *ab initio* CC/CBS(d, t) points while the dotted lines represent the dissociation energy limits predicted from $V^{(2+3)}(\mathbf{R})$.

required symmetrized sums of monomials and make $V^{(4)}(\mathbf{R})$ [eqn (9)] invariant with respect to all permutations of like atoms.^{45,46}

Like electronic structure theory,⁵¹ each y_p in eqn (9) is in CHIPR expanded as a distributed-origin contracted basis set^{45,46}

$$y_p = \sum_{\alpha=1}^M c_{\alpha} \phi_{p,\alpha}, \quad (10)$$

where $\phi_{p,\alpha}$ is expressed either as^{45,46}

$$\phi_{p,\alpha}^{[1]} = \operatorname{sech}^{\eta}(\gamma_{p,\alpha} \rho_{p,\alpha}), \quad (11)$$

or

$$\phi_{p,\alpha}^{[2]} = \left[\frac{\tanh(\beta R_p)}{R_p} \right]^{\sigma} \operatorname{sech}^{\eta}(\gamma_{p,\alpha} \rho_{p,\alpha}). \quad (12)$$

In the above equations, $\rho_{p,\alpha} = R_p - R_{p,\alpha}^{\text{ref}}$ defines the displacement coordinate R_p from the α th primitive's origin $R_{p,\alpha}^{\text{ref}}$, $\gamma_{p,\alpha}$ are non-linear parameters and $\eta = 1$, $\sigma = 6$ and $\beta = 1/5$ are constants.^{45,46} As usual,⁴⁷ both $\phi_{p,\alpha}^{[1]}$ and $\phi_{p,\alpha}^{[2]}$ were employed in eqn (10), with the latter appearing only once as the last term in the summation. Note that all distributed origins $R_{p,\alpha}^{\text{ref}}$ in eqn (11) and (12) are assumed related by⁴⁵

$$R_{p,\alpha}^{\text{ref}} = \zeta (R_p^{\text{ref}})^{\alpha-1}, \quad (13)$$

where ζ and R_p^{ref} are adjustable parameters.

The first step in CHIPR consists of calibrating the above contracted basis sets [eqn (10)]. For this, we have performed 1D CC/CBS(d, t) cuts along the C–C and C–H bond lengths of a previously selected $c\text{-}C_3\text{H}$ reference geometry; this is made up of a D_{3h} structure of C_3 ($R_{\text{CC}} = 2.596a_0$) and the experimental²⁷

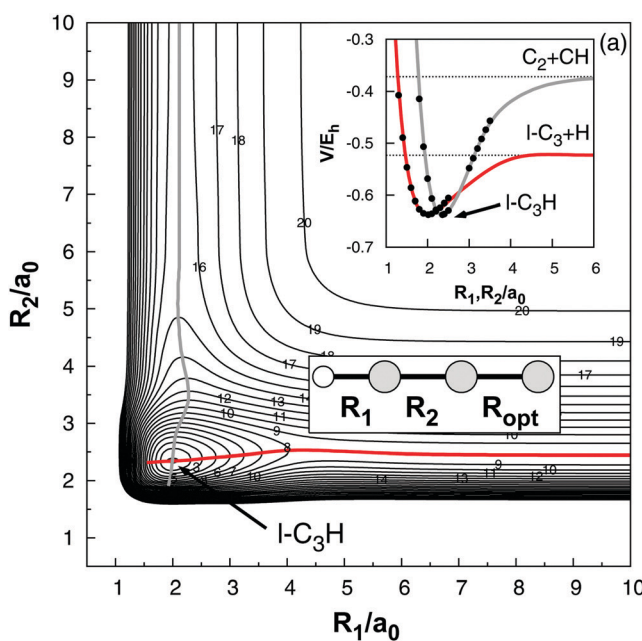
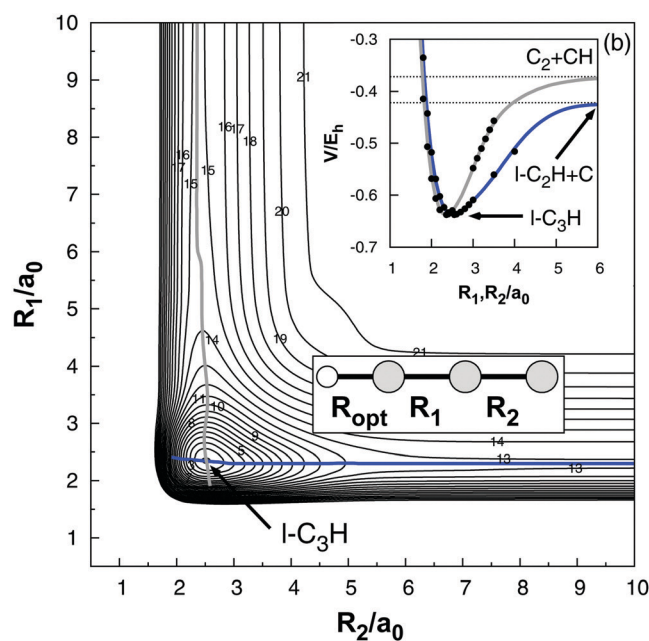


Fig. 6 Contour plots for the CH and C_2 collinear reactions yielding (a) $\text{\texteta-}C_3 + H$ and (b) $\text{\texteta-}C_2\text{H} + C$. Contours are equally spaced by $0.015E_h$, starting at $-0.65E_h$. In the insets, the corresponding optimized 1D cuts are shown. Solid dots indicate *ab initio* CC/CBS(d, t) points while dotted lines represent the dissociation energy limits predicted from $V^{(2+3)}(\mathbf{R})$. The zero of energy is set relative to the infinitely separated atoms.



CH bond distance ($R_{\text{CH}} = 2.033a_0$). With the above data, the parameters of eqn (10)–(13) have then been determined from a fit to the resulting four-body energies. The final bases, referred to as CHb8 and CCb8, are depicted in Fig. 2. Note that their corresponding non-linear parameters have been optimized only once and are kept fixed in all subsequent steps.

Having CHb8 and CCb8, the second step in CHIPR is the determination of the polynomial coefficients in eqn (9). To accomplish this, we have first set all c_x 's to their previously optimized values and the C coefficients [eqn (9)] to unity. The fitting solution so found was then employed as an initial guess for a subsequent optimization in which all parameters (including c_x 's) were varied freely. The final optimized contracted bases are also shown in Fig. 2. For the weights (W), we employ the following function

$$W(E) = \begin{cases} 2 & \text{if min, ts, MEP} \\ 3/2 & \text{if } E \leq E_0 \\ 1 - \tanh[\beta(\Delta E)] & \text{if } E > E_0, \end{cases} \quad (14)$$

where $\Delta E = E - E_{\min}$, $\beta = 1/2$, $E_{\min} = -0.645E_h$ and $E_0 = -0.62E_h$, with larger weights attributed to minima (min), transition states (ts) and minimum energy paths (MEPs).

With such an approach, all 42 538 *ab initio* points could be least-squares fitted to eqn (9) with a root mean square deviation (rmsd) of 8.0 kJ mol⁻¹. This involves a total of 360 linear coefficients in the polynomial expansion ($L = 10$), and basis set contractions of the order $M = 3$ (8 parameters each), thence amounting to 113 fitted points per parameter; see the ESI† to

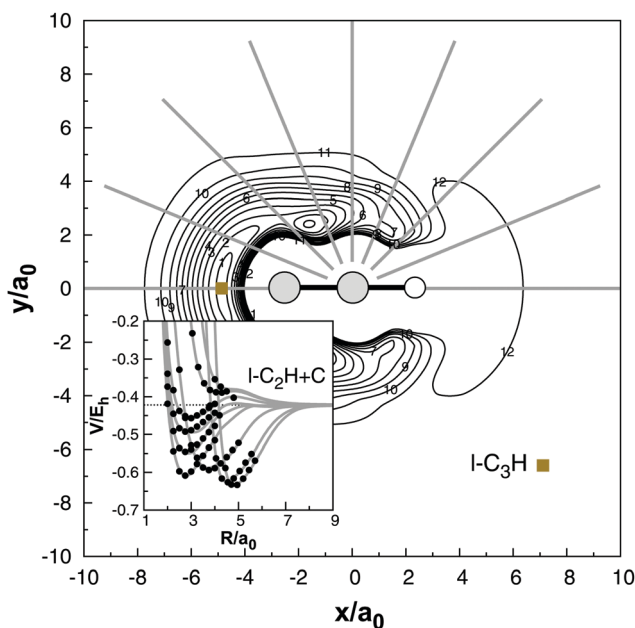


Fig. 7 Contour plot for a C atom moving around a partially relaxed η -C₂H which lies along the x axis with the C atom kept at the origin. Contours are equally spaced by $0.02E_h$ starting at $-0.65E_h$. The zero of energy is set relative to the infinitely separated atoms. Shown in the inset are the corresponding optimized 1D cuts. Solid dots indicate *ab initio* CC/CBS(d,t) points while the dotted line represents the dissociation energy limit predicted from $V^{(2+3)}(R)$.

assess the numerical coefficients of all parameters outgoing from the fit. Shown in Fig. S2 (ESI†) is the sensitivity of the energy fit with respect to the various parameters. In particular, this shows how the second derivative of χ^2 [sum of the squared deviations of eqn (9) from the *ab initio* computed energies] varies for the first row that interrelates the first to all other polynomial coefficients. As one might expect, the sensitivity generally decreases with the total order of the polynomial coefficient. In turn, Table 2 displays the stratified rmsd and CC diagnostic tests^{66–68} using the AVTZ basis set (see also Fig. S3–S5 of the ESI†), while Fig. 3 shows the distribution of errors in the fitted data set. As noted, although the stratified diagnostics deviate slightly from their recommended values (in accordance

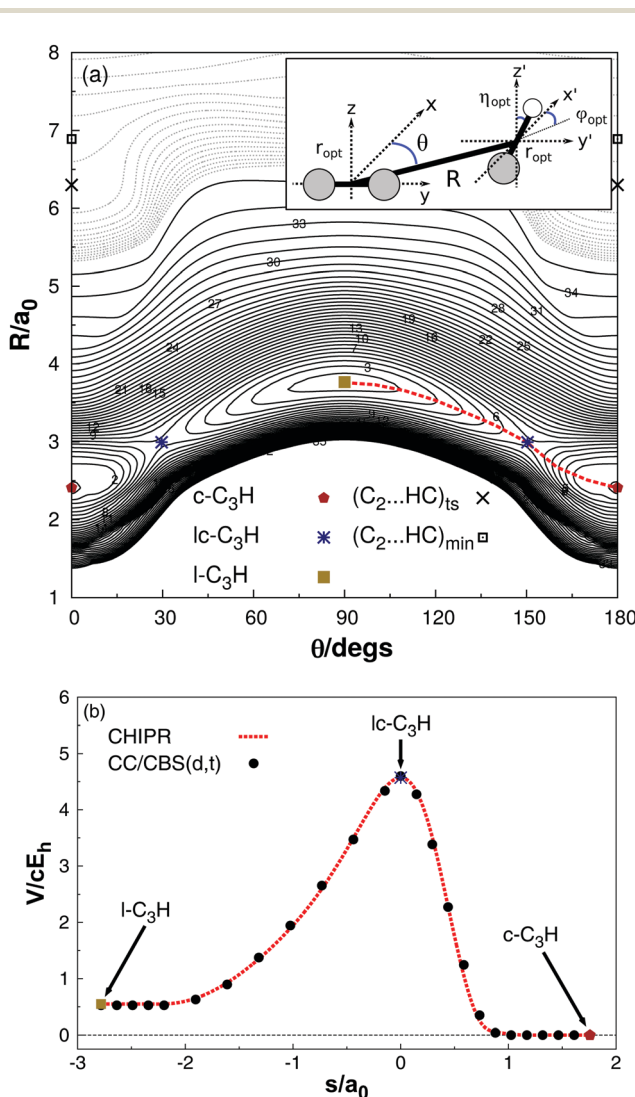


Fig. 8 (a) Contour plot for CH moving around a C₂ diatom with the center-of-mass fixed at the origin. All degrees of freedom but R and θ are partially relaxed as shown in the inset. Black solid and gray dotted contours are equally spaced by 0.0075 and 0.00075 E_h starting at -0.65 and $-0.385E_h$, respectively. The zero of energy is set relative to the infinitely separated atoms. (b) Minimum energy path (s is the reaction coordinate in mass-scaled a.u.) for isomerization between c-C₃H and η -C₃H via the transition state of /c-C₃H. The zero of energy corresponds to c-C₃H.

with previous results³⁹), *i.e.*, $T_1 \leq 0.02$,⁶⁶ $D_1 \leq 0.05$ ⁶⁷ and $T_1/D_1 \approx 1/\sqrt{2}$,⁶⁸ the use of multireference electron correlation methods for C_3H would make the task of calculating its global PES computationally unaffordable. Indeed, the relative cost between single point MRCI+Q/CBS(D, T) and CC/CBS(d, t) calculations amounts to ≈ 1200 . This justifies our cost-effective way.

4 Features of PESs

All major features of the CHIPR PES are depicted in Fig. 4–9; for the properties of its stationary points, see Tables 3–6, where the most recent/representative results available from the literature^{12,21,26,27,39–42,69} are also shown.

Accordingly, the predicted global minimum on the ground-state doublet of the PES corresponds to a cyclic C_{2v} geometry, $c\text{-}\text{C}_3\text{H}$ (Fig. 4). As shown in Table 4, its predicted structural parameters are in excellent agreement with the ones observed *via* microwave spectroscopy.²⁷ A close agreement is also found between the CHIPR's $c\text{-}\text{C}_3\text{H}$ data and the recently reported CC-F12/AVTZ results of Bennedjai *et al.*⁴⁰ as well as the predicted QFF geometry of Bassett and Fortenberry.³⁹ The latter includes, in addition to CBS energies, contributions from core–core/core–valence electron correlation and scalar relativistic effects.³⁹ Moreover, with the exception of the C–C asymmetric stretching mode (ω_4), all harmonic frequencies are well reproduced by CHIPR. Note that ω_4 corresponds to the $c\text{-}\text{HC}_3(\tilde{\chi}^2\text{B}_2/1^2\text{A}')$

symmetry lowering (from C_{2v} to C_s) which, according to previous work,^{27,36,38} is subject to vibronic mixing with the next $2^2\text{A}_1/2^2\text{A}'$ electronic state. Table 3 gives our best estimate of this excitation energy, namely ≈ 113.2 kJ mol^{−1} above $\tilde{\chi}^2\text{B}_2$. For the benefit of the reader, we also include exploratory estimates of stationary structures for the lowest 7 excited states of $c/\ell\text{-}\text{HC}_3$ (note that only geometries close to the one of equilibrium $c\text{-}\text{HC}_3$ or $\ell\text{-}\text{HC}_3$ have been explored). Although the experimental ν_4 value is itself largely questioned³⁹ (it is derived from rotational distortions rather than vibrational observations;²⁷ this is also true for the other experimental IR bands²⁶), difficulties in describing ω_4 seem to appear also in the case of CC-F12 wave functions (see Table 4). Nevertheless, as noted in various occasions,^{38–40} extrapolations to the CBS limit tend to favor the highest symmetry C_{2v} structure over the (double minimum) C_s distorted ones. As shown in Fig. 4, the isomerization between the three symmetry-equivalent $c\text{-}\text{C}_3\text{H}$ structures occurs *via* a (thus far unreported) C_{2v} transition state of $cc\text{-}\text{C}_3\text{H}$. This form is predicted from CHIPR to be located 197.7 kJ mol^{−1} above $c\text{-}\text{C}_3\text{H}$ with an imaginary frequency of 1693.9 cm^{−1} along the H wagging motion (through $c\text{-}\text{C}_3$'s center-of-mass). The corresponding classical barrier heights calculated from CC/CBS(d, t) and MRCI+Q/CBS(D, T) protocols [for the description of the latter, see ref. 60] are estimated to be 194.2 and 188.8 kJ mol^{−1}, respectively (Table 5). In fact, a close look at inset (b) of Fig. 4 shows that the CHIPR form reproduces accurately the MEP at the CC/CBS(d, t) level.

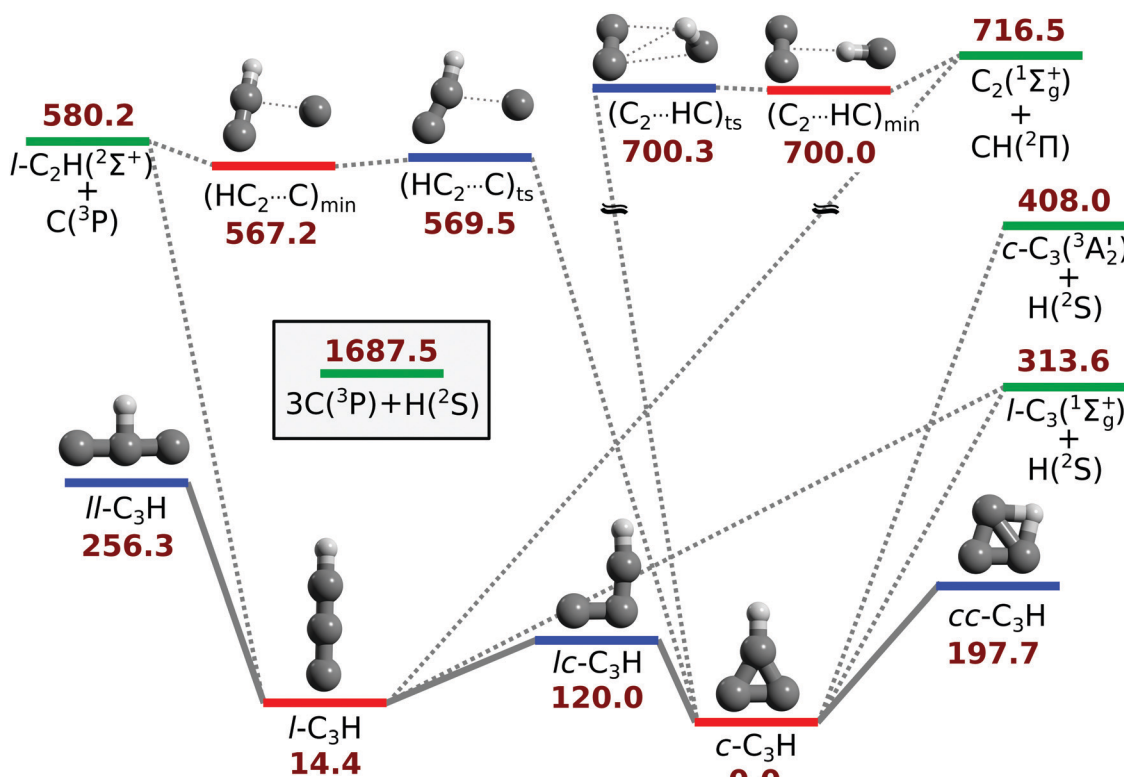


Fig. 9 Pathways connecting the stationary points on the CHIPR PES. All energies (in kJ mol^{−1}) refer to the global $c\text{-}\text{C}_3\text{H}$ minimum. Dotted lines connect dissociative channels (in green), while solid ones connect isomeric structures (red for minima, blue for transition states).

Table 3 Vertical excitation energies (T_e in kJ mol^{-1}) for some low-lying excited states of c - and ℓ - C_3H as obtained from two-state CASSCF(13,13)-MRCI+Q/CBS(D,T)⁶⁰ calculations using the C_{2v} point group. The electronic states are labeled according to C_{2v} irreducible representations with the corresponding correlations with $C_{\infty v}$ and/or C_s also given in parenthesis. The energies are calculated at the corresponding experimental (ground-state) equilibrium geometries^{22,27} (see also Table 4)

$c\text{-C}_3\text{H}$			$\ell\text{-C}_3\text{H}$		
State	Γ_{el}^a	T_e^b	State	Γ_{el}^a	T_e^b
1	$^2\text{B}_2(^2\text{A}')$	0.0	1	$^2\text{B}_2(^2\Pi/2\text{A}')$, $^2\text{B}_1(^2\Pi/2\text{A}'')$	14.5
2	$^2\text{A}_1(^2\text{A}')$	113.2	2	$^2\text{A}_1(^2\Delta/2\text{A}')$, $^2\text{A}_2(^2\Delta/2\text{A}''')$	281.0
	$[96.8 \pm 1.2]^c$			$[268]^d$	
3	$^2\text{B}_1(^2\text{A}''')$	326.3	3	$^2\text{A}_2(^2\Sigma^-/2\text{A}')$	311.9
4	$^2\text{A}_2(^2\text{A}''')$	369.3	4	$^2\text{A}_1(^2\Sigma^+/2\text{A}')$	346.1
5	$^2\text{A}_2(^2\text{A}''')$	437.5	5	$^2\text{B}_2(^2\Pi/2\text{A}')$, $^2\text{B}_1(^2\Pi/2\text{A}''')$	370.7
6	$^2\text{B}_1(^2\text{A}''')$	439.3			
7	$^2\text{A}_1(^2\text{A}')$	478.2			
8	$^2\text{B}_2(^2\text{A}')$	678.2			

^a Electronic symmetry species. ^b MRCI+Q/CBS(D,T) values relative to the ground-state $c\text{-C}_3\text{H}$ minimum. ^c Experimental gas-phase values reported in ref. 26. ^d Experimental gas-phase $^2\Pi \rightarrow ^2\text{A}''(^2\Delta)$ transition reported in ref. 28.

Besides $c\text{-C}_3\text{H}$, CHIPR predicts the linear isomer $\ell\text{-C}_3\text{H}$ to be a local minimum in the ground-state of the PES lying 14.4 kJ mol^{-1} above the cyclic structure; see Fig. 5–7. As shown in Table 4, the corresponding energy differences at the CC/CBS(d,t), CC-F12/AVTZ⁴⁰ and MRCI+Q/CBS(D,T) levels are

11.8 , 15.4 and 5.3 kJ mol^{-1} , respectively. Note that the CHIPR's $\ell\text{-C}_3\text{H}$ structural parameters agree well with the experimental (vibrationally averaged) r_0 values reported by Kanada *et al.*²² [at experimental geometries, our best estimate places $\ell\text{-C}_3\text{H}$ about 14.5 kJ mol^{-1} above $c\text{-C}_3\text{H}$ (Table 3)]. Discrepancies, however, should *a priori* be expected in the description of the C–C–H and C–C–C degenerate bending modes (Table 4) whose vibrational angular momentum is shown^{22,23} to couple with the $^2\Pi$ (total) electronic angular momentum. As first remarked by Kanada *et al.*²² and later by Perić *et al.*,⁴¹ such a strong RT effect makes the lowest $^2\text{A}'$ PES very flat along w_4 with the appearance of a quasi-linear C_3H molecule, depending on the chosen *ab initio* method; see, *e.g.*, Table S4 (ESI†) for the truncated-space CASSCF/MRCI+Q estimates. Here, in accordance with the recent CC-F12⁴⁰ calculations and ref. 28, the extrapolations to the CBS limit tend to favor the highest symmetry $C_{\infty v}$ species (Table 4). Suffice to add that the predicted structural parameters and harmonic frequencies for $\ell\text{-C}_3\text{H}$ are also in close agreement with the ones derived from the local $^2\text{A}'$ PES studied by Perić *et al.*⁴¹ Note that, as for $c\text{-C}_3\text{H}$, the experimental $\ell\text{-C}_3\text{H}$'s IR bands but $\nu_4(^2\Sigma^{\mu})$ are largely uncertain.^{21,25,26,69}

Clearly visible from Fig. 5 is the presence of a T-shaped (C_{2v}) transition state, hereafter denoted as $\ell\ell\text{-C}_3\text{H}$, which is responsible for the degenerate isomerization between symmetry-equivalent $\ell\text{-C}_3\text{H}$ structures; its imaginary frequency amounts to 1111.7 cm^{-1} and points toward the H wagging motion through $\ell\text{-C}_3$

Table 4 Structural parameters (distances in a_0 , angles in deg) and harmonic (w_i) frequencies (in cm^{-1}) of minima on the C_3H ground-state PES. Energies (ΔE) in kJ mol^{-1} refer to global $c\text{-C}_3\text{H}$ minima

Structure	Property ^a	CHIPR ^b	CC ^c	MRCI+Q ^d	CC-F12 ^e	QFF ^f	Exp.
$c\text{-C}_3\text{H}$	R_{HC_1}	2.034	2.038	2.012	2.039	2.036	2.033^g
	$R_{\text{C}_1\text{C}_2}$	2.587	2.526	2.531	2.600	2.595	2.596^g
	$R_{\text{C}_2\text{C}_3}$	2.557	2.622	2.654	2.608	2.590	2.602^g
	$\angle \text{HC}_1\text{C}_2$	150.4	156.5	157.0	149.9	150.1	149.9^g
	$\angle \text{C}_1\text{C}_2\text{C}_3$	60.4	64.0	64.5	59.9	60.1	59.9^g
	w_1 (CH stretch)	3052.9	3269.9	3433.5	3246.0	3256.8	
	w_2 (CC sym. stretch)	1381.5	1159.4	1108.8	1578.0	1588.6	1613 ± 25^h
	w_3 (CCH sym. bend)	1754.7	1606.0	1566.8	1214.0	1219.5	1161 ± 25^h
	w_4 (CC asym. stretch)	1327.9	919.4	884.8	2639.0	619.5	$508 \pm 25^{g,h}$
	w_5 (H wag)	951.0	894.9	840.6	900.0	1224.8	
$\ell\text{-C}_3\text{H}$	w_6 (H out of plane)	878.8	819.2	713.8	858.0	863.1	
	Spg	C_{2v}	C_s	C_s	C_{2v}	C_{2v}	C_{2v}^g
	ΔE	0.0	0.0 (0.0)	0.0 (0.0)	0.0		
	R_{HC_1}	1.994	2.017	2.033	2.013	2.022	1.922^i
	$R_{\text{C}_1\text{C}_2}$	2.346	2.366	2.367	2.351	2.372	2.370^i
	$R_{\text{C}_2\text{C}_3}$	2.519	2.539	2.578	2.538	2.561	2.506^i
	$\angle \text{HC}_1\text{C}_2$	180.0	164.4	175.2	180.0	180.0	
	$\angle \text{C}_1\text{C}_2\text{C}_3$	180.0	175.9	178.2	180.0	180.0	
	w_1 (CH stretch)	3372.5	3403.7	3543.7	3428.0	3600.0	3238^j
	w_2 (CCC asym. stretch)	1856.5	1844.4	1807.1	1870.0	1830.0	$1839 \pm 10, 1824.7^j$
	w_3 (CCC sym. stretch)	1094.5	1137.7	1137.7	1136.0	1160.0	$1167, 1159.8^j$
	w_4 (CCH bend)	247.7	223.9, 236.8	219.6, 297.6	230.0	202.0	$600, 20.3^l$
	w_5 (CCC bend)	302.6	371.7	355.8	371.0	374.0	300^k
	Spg	$C_{\infty v}$	C_s	C_s	$C_{\infty v}$	$C_{\infty v}$	$C_{\infty v}^k$
	ΔE	14.4	7.3 (11.8)	0.8 (5.3)	15.4		

^a This work. spg stands for the symmetry point group. ^b This work. ^c This work, with the AVTZ basis set. ΔE values in parenthesis are CC/CBS(d,t) at CHIPR stationary points. ^d This work, with the MRCI+Q/CBS(D,T) at CHIPR stationary points. Geometries at the single-state CASSCF(13,13)/AVTZ level. ΔE values in parenthesis are MRCI+Q/CBS(D,T) at CHIPR stationary points; see ref. 60 for the CBS protocol. ^e Ref. 40, with the AVTZ basis set. ^f Local PESs of ref. 39 (for $c\text{-C}_3\text{H}$) and ref. 41 (for $\ell\text{-C}_3\text{H}$). ^g Ref. 27 and 12. ^h Ref. 26. Gas-phase values. ⁱ Ref. 22. Gas-phase values. ^j Ref. 69 and 25. Measured in the Ar matrix. ^k Ref. 21. Estimated fundamentals in the absence of Renner-Teller and spin-orbit effects. ^l Ref. 21. $\nu_4(^2\Sigma^{\mu})$ fundamental bands.

Table 5 Attributes of transition states on the C₃H ground-state PES. Properties and units as in Table 4

Property ^a	cc-C ₃ H			ℓℓ-C ₃ H		
	CHIPR ^b	CC ^c	MRCI+Q ^d	CHIPR ^b	CC ^c	MRCI+Q ^d
R _{HC₁}	2.361	2.443	2.461	2.226	2.142	2.150
R _{C₁C₂}	2.540	2.537	2.555	2.533	2.559	2.589
R _{C₁C₃}	2.540	2.537	2.555	5.065	5.081	5.096
∠ HC ₁ C ₂	103.5	101.7	100.8	89.1	96.8	100.2
∠ C ₁ C ₂ C ₃	73.2	76.6	77.4	0.9	6.8	10.2
w ₁	1693.9i	1676.2i	1616.9i	1111.7i	649.0i	1115.8i
w ₂	751.1	637.7	616.5	164.0	91.2	307.2
w ₃	879.9	797.3	840.1	350.1	302.6	429.9
w ₄	1177.2	1348.1	1325.8	1094.5	1060.7	1023.3
w ₅	2087.2	1630.1	1584.5	1512.8	1494.7	1279.0
w ₆	2380.0	2242.0	2189.6	2581.7	2812.6	2754.3
Spg	C _{2v}	C _{2v}	C _{2v}	C _{2v}	C _{2v}	C _{2v}
ΔE	197.7	185.3 (194.2)	178.3 (188.8)	256.3	243.7 (258.1)	233.9 (251.1)
ℓc-C ₃ H						
Property ^a	CHIPR ^b	CC ^c	MRCI+Q ^d	CC ^e		
R _{HC₁}	2.036	2.046	2.068		2.050	
R _{C₁C₂}	2.446	2.494	2.514		2.481	
R _{C₁C₃}	2.586	2.524	2.542		2.502	
∠ HC ₁ C ₂	173.6	140.7	140.2		139.9	
∠ C ₁ C ₂ C ₃	94.0	90.2	89.1		89.4	
d _{HC₁C₂C₃}	180.0	129.4	131.8		132.3	
w ₁	796.1i	1343.2i	1271.8i			
w ₂	160.7	618.0	586.5			
w ₃	443.6	690.1	704.2			
w ₄	1265.1	1394.2	1364.8			
w ₅	1523.9	1517.6	1479.7			
w ₆	3039.5	3216.5	3099.4			
Spg	C _s	C ₁	C ₁		C ₁	
ΔE	120.0	115.7 (122.1)	110.0 (123.8)		114.6	

^a This work. spg stands for the symmetry point group. ^b This work. ^c This work, calculated with the AVTZ basis set. ΔE values in parenthesis are CC/CBS(*d,t*) at CHIPR stationary points. ^d This work, calculated using the AVTZ basis set. Geometries at the single-state CASSCF(13,13)/AVTZ level. ΔE values in parenthesis are MRCI+Q/CBS(*D,T*) at CHIPR stationary points; see ref. 60 for the CBS protocol. ^e Ref. 42, calculated at the CC/6-311+G(3df,2p)//B3LYP/6-311G(d,p) level.

center-of-mass. Such a hitherto unreported form lies about 241.9 and 256.3 kJ mol⁻¹ above ℓ-C₃H and c-C₃H, respectively (Table 5). The corresponding isomerization barriers predicted from CC/CBS(*d,t*) and MRCI+Q/CBS(*D,T*) protocols are 246.3 and 245.8 kJ mol⁻¹. Again, Fig. 5 [inset (b)] evinces the reliability of the CHIPR form in reproducing the CC/CBS(*d,t*) MEP for this process. In turn, as noted in Fig. 8(a) and (b), the isomerization between c-C₃H and ℓ-C₃H occurs via ℓc-C₃H transition states^{14,42} whose imaginary frequency (of 796.1 cm⁻¹) points along the C–C bond breaking/forming process; see Fig. 9 to assess all geometries of the stationary structures discussed here. The classical barrier height is predicted to be 120.0 kJ mol⁻¹ relative to c-C₃H; the corresponding CC/CBS(*d,t*) and MRCI+Q/CBS(*D,T*) values are 122.1 and 123.8 kJ mol⁻¹, respectively.

Fig. 9 summarizes in a comprehensive way all major topographical attributes of the CHIPR form reported here. Fig. 4–8 accurately reproduce all known valence features of the PES, their isomerization pathways and permutational symmetries by built-in construction, and also describes in a physically reasonable manner all long-range structures and the correct asymptotic behavior at dissociation. This is no doubt achieved by the use of the MBE/CHIPR methods^{10,45,46} with appropriate $\mathcal{P}_g^{(ij,k,l,m,n)}$ operators in eqn (9). Indeed, as Fig. 8, 9 and Table 6 show, CHIPR also

predicts long-range stationary points [(HC₂···C)_{min}, (HC₂···C)_{ts}, (C₂···HC)_{min} and (C₂···HC)_{ts}] with structural parameters and energetics in close agreement with the ones obtained at CASSCF/AVTZ and MRCI+Q/CBS(*D,T*) levels. Such forms arise from the perpendicular attack of C to the central C atom of ℓ-C₂H and CH to the C₂ diatom, both toward c-C₃H formation (see Fig. 9). In addition, Fig. 6 and 9 show that the formation of ℓ-C₃H is barrierless for the collinear reactions of C₂ + CH, ℓ-C₃ + H and C + ℓ-C₂H, in accordance with ref. 42. Moreover, the c-C₃H adduct is formed without any barrier by the perpendicular approach of H to both c-C₃(³A₁) and ℓ-C₃(¹Σ_g⁺) [in this case, the attack involves more than one reaction coordinate];⁴² the overall exothermicities of all such processes can be assessed from Fig. 9.

5 Preliminary QCT dynamics study

In this section, we test the reliability of the CHIPR form through preliminary calculations of rate constant for the reaction C₂(*v,j*) + CH(*v',j'*) → C₃ + H by running quasi-classical trajectories (QCT)⁷⁰ on the novel PES; a locally modified version of the VENUS96C code⁷¹ has been employed throughout. All calculations used a time step of 0.075 fs with the reactants initially separated

Table 6 Long-range attributes of the C₃H ground-state PES. Properties and units as in Table 4

Property ^a	(HC ₂ ···C) _{min}		(HC ₂ ···C) _{ts}	
	CHIPR ^b	MRCI+Q ^c	CHIPR ^b	MRCI+Q ^c
R _{HC₁}	2.008	1.938	2.004	1.940
R _{C₁C₂}	2.281	2.081	2.317	2.195
R _{C₁C₃}	6.960	6.459	6.873	5.980
∠ HC ₁ C ₂	179.0	180.0	165.2	150.0
∠ C ₁ C ₂ C ₃	68.0	59.5	52.8	48.0
w ₁	119.8	111.7	310.3i	149.0i
w ₂	138.8	211.5	154.9	165.4
w ₃	403.5	425.0	372.3	329.8
w ₄	444.9	430.8	539.9	420.9
w ₅	1817.0	2060.0	1384.2	1907.8
w ₆	3430.1	3463.9	3284.3	3476.2
Spg	C _s	C _s	C _s	C _s
ΔE	567.2	552.0 (568.2)	569.5	555.0 (578.5)
Property ^a	(C ₂ ···HC) _{min}		(C ₂ ···HC) _{ts}	
	CHIPR ^b	MRCI+Q ^c	CHIPR ^b	MRCI+Q ^c
R _{HC₁}	2.104	1.952	2.118	1.918
R _{C₁C₂}	7.533	7.325	7.108	6.808
R _{C₁C₃}	2.439	2.472	2.443	2.493
∠ HC ₁ C ₂	9.3	15.3	60.9	70.3
∠ C ₁ C ₂ C ₃	80.7	70.5	80.1	67.5
d _{HC₁C₂C₃}	0.0	0.0	-80.4	-85.2
w ₁	92.7	108.8	88.9i	193.5i
w ₂	171.7	268.5	100.4	61.5
w ₃	200.3	298.9	122.1	114.3
w ₄	217.1	313.0	215.7	303.0
w ₅	844.5	1790.0	1071.4	1615.4
w ₆	3016.7	2988.2	2926.3	2859.3
Spg	C _{2v}	C _{2v}	C _{2v}	C _{2v}
ΔE	700.0	695.0 (715.6)	700.3	699.4 (716.1)

^a This work. spg stands for the symmetry point group. ^b This work.

^c This work, calculated with the AVTZ basis set. Geometries at the single-state CASSCF(13,13)/AVTZ level. ΔE values in parenthesis are MRCI+Q/CBS(D,T) at CHIPR stationary points; see ref. 60 for the CBS protocol.

by 8 Å, while the maximum value of the impact parameter is $b_{\max} = 6$ Å as optimized by trial and error. Average reaction cross sections were then obtained (for a given temperature T) as⁷⁰ $\langle \sigma_R(T) \rangle = \pi b_{\max}^2 N_R / N$, and the 68% associated errors by $\Delta \langle \sigma_R(T) \rangle = \langle \sigma_R(T) \rangle [(N - N_R)/(NN_R)]^{1/2}$, where N_R is the number of reactive trajectories out of a total of N (10⁴ per temperature) that were run. In turn, thermal rate constants for the formation of C₃ + H were calculated as⁷⁰

$$k(T) = g_e \left(\frac{8k_B T}{\pi \mu_{\text{CH+C}_2}} \right)^{1/2} \langle \sigma_R(T) \rangle, \quad (15)$$

with the estimated 68% error being given by $\Delta k(T) = k(T)[(N - N_R)/(NN_R)]^{1/2}$; k_B is the Boltzmann constant, $\mu_{\text{CH+C}_2}$ is the reduced mass of the reactants and $g_e = 1/12$ is the electronic degeneracy factor. The calculated results for temperatures up to 4000 K are shown in Fig. 10 and 11.

To further explore the dependence of $\langle \sigma_R \rangle$ with respect to temperature, we have considered the following model function⁷⁴

$$\langle \sigma_R(T) \rangle = (a + bT + cT^2)T^n \exp(-mT), \quad (16)$$

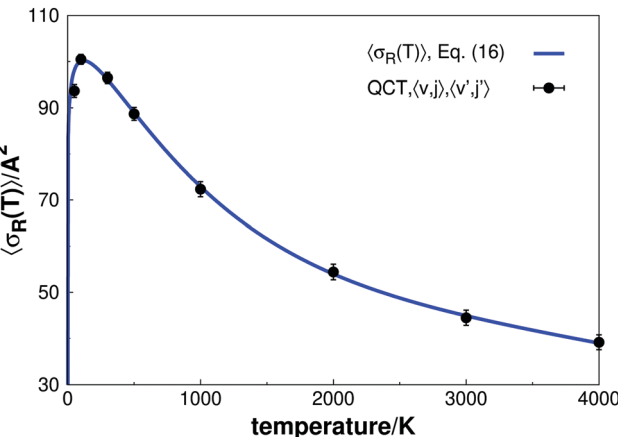


Fig. 10 Cross sections and associated error bars as a function of temperature. The line shows the curve fitted to QCT data, eqn (16). For clarity, the results are shown with 99.6% [3σ ≡ 3Δ⟨σ_R(T)⟩] error bars.

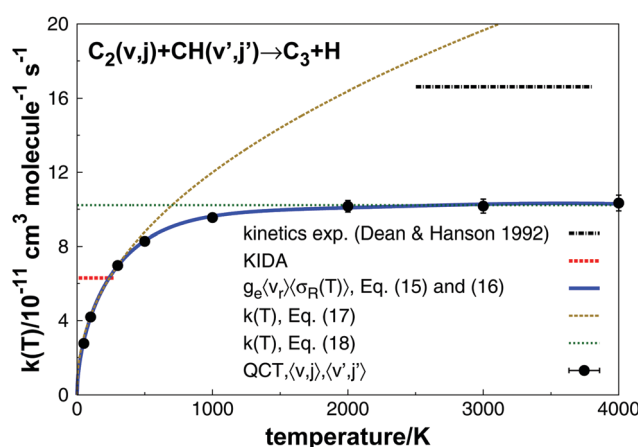


Fig. 11 Rate constants and associated error bars for the C₂ + CH reaction at temperatures up to 4000 K. Also shown are the experimental estimates of Dean and Hanson⁷² and available data from KIDA kinetics database.⁷³ The lines show the predicted QCT thermally averaged results from the excitation function in eqn (16)–(18). For clarity, the QCT results are shown with 99.6% [3σ ≡ 3Δk(T)] error bars.

Table 7 Parameters for ⟨σ_R(T)⟩ in eqn (16)

Parameter	Value ^a
a/Å ² K ⁻ⁿ	7.52 (+1)
b/Å ² K ⁻⁽¹⁺ⁿ⁾	-1.25 (-2)
c/Å ² K ⁻⁽²⁺ⁿ⁾	7.52 (-6)
n	7.51 (-2)
m/K ⁻¹	4.85 (-4)

^a The power of 10 is in parenthesis.

where a , b , c , n , and m are parameters to be adjusted to the QCT calculated cross-sections; they are numerically defined in Table 7, with the final form of ⟨σ_R(T)⟩ plotted in Fig. 10. In turn, the predicted thermally averaged $k(T)$'s arising from substituting eqn (16) into (15) are shown in Fig. 11. Clearly, the model function of eqn (16) accurately fits the calculated

$\langle\sigma_R(T)\rangle$'s. As is visible from Fig. 10, the excitation function at $T \approx 100$ K displays a maximum at very low collision energies, although no apparent barrier exists along the minimum energy path for the reaction. A possible implication is that other regions of the PES close to the minimum energy path are sampled by the trajectories, thus requiring a tiny barrier to be overcome. As seen, a good agreement is found between the calculated and predicted rate constants (see Fig. 11). In the high temperature range ($2500 \leq T/K \leq 3800$), the QCT calculated rate constants are predicted to be about 38% lower than the experimental estimates of Dean and Hanson.⁷² Conversely, at ≈ 280 K, our calculations agree remarkably well with the value of $6.30 \times 10^{-11} \text{ cm}^3 \text{ molecule}^{-1} \text{ s}^{-1}$ (believed valid for the range of 10–280 K) recommended by the KIDA kinetics database;⁷³ however, this clearly diverges for lower T . In fact, as seen from Fig. 11, the calculated rate constant is predicted to increase as a function of temperature, thus showing a positive slope. Specifically, it is well approximated by (in $\text{cm}^3 \text{ molecule}^{-1} \text{ s}^{-1}$)

$$k(T) = 6.98 \times 10^{-11} (T/300)^{0.45} \quad (17)$$

for temperatures up to ≈ 500 K. A similar dependence ($T^{0.6}$) has also been found experimentally for the case of the barrierless reaction between C_2 and the (CH-congenere) N atom.⁷⁵ However, in high temperature regimes, it is predicted to be approximately constant,

$$k(T) \cong 1.02 \times 10^{-10} \text{ cm}^3 \text{ molecule}^{-1} \text{ s}^{-1} \quad (18)$$

over the 2000–4000 K interval; eqn (17) and (18) are also plotted in Fig. 11. A final remark to note is that at 10 K, a temperature of relevance in cold dense clouds, the model function of eqn (16) yields [using eqn (15)] a rate constant of $1.18 \times 10^{-11} \text{ cm}^3 \text{ molecule}^{-1} \text{ s}^{-1}$ for the reaction $\text{C}_2(v,j) + \text{CH}(v',j') \rightarrow \text{C}_3 + \text{H}$. This is compared with the value of¹⁵ $2.23 \times 10^{-10} \text{ cm}^3 \text{ molecule}^{-1} \text{ s}^{-1}$ (at 10 K) for the $\text{C} + \text{C}_2\text{H}_2 \rightarrow \text{H}_2 + \text{C}_3$ reaction, a well established (neutral-neutral) source of carbon trimer in the ISM.^{15,42}

6 Conclusions

We have reported the first global PES for the ground-state doublet C_3H using accurate CBS extrapolated *ab initio* energies and the CHIPR method for modelling. The novel PES is based on a MBE-type development with the two-body and three-body energy terms from previously reported double-MBE potentials for $\text{C}_2\text{H}(^2\text{A}')$ ⁶¹ and $\text{C}_3(^1\text{A}', ^3\text{A}')$,^{60,62} while the effective four-body energy term is modelled using the CHIPR formalism for AB_3 -type tetratomics. The final form reproduces accurately all known stationary structures of HC_3 and their interconversion pathways, some unreported thus far to the best of our knowledge. Besides describing properly long-range interactions at all asymptotic channels and permutational symmetry by built-in construction, the PES reproduces reasonably well all exothermicities at dissociation regions – the best one can possibly afford with the above two- and three-body potentials and our cost-effective *ab initio* approach. By running exploratory quasi-classical trajectory

calculations for the reaction $\text{C}_2 + \text{CH} \rightarrow \text{C}_3 + \text{H}$, thermalized rate coefficients for temperatures up to 4000 K are also reported.

Conflicts of interest

There are no conflicts to declare.

Acknowledgements

This work is supported by the Fundação para a Ciência e a Tecnologia and Coimbra Chemistry Centre, Portugal, in the framework of the project “MATIS – Materiais e Tecnologias Industriais Sustentáveis” (reference: CENTRO-01-0145-FEDER-000014), co-financed by the European Regional Development Fund (FEDER), through the “Programa Operacional Regional do Centro” (CENTRO2020) program. C. M. R. R. also thanks the CAPES Foundation (Ministry of Education of Brazil) for a scholarship (BEX 0417/13-0). The support from A. J. C. V. from the China's Shandong Province “Double-Hundred Talent Plan” (2018) is also appreciated.

References

- 1 B. A. McGuire, *ApJS*, 2018, **239**, 17.
- 2 R. I. Kaiser, *Chem. Rev.*, 2002, **102**, 1309–1358.
- 3 I. W. M. Smith, E. Herbst and Q. Chang, *Mon. Notices Royal Astron. Soc.*, 2004, **350**, 323–330.
- 4 I. W. M. Smith, A. M. Sage, N. M. Donahue, E. Herbst and D. Quan, *Faraday Discuss.*, 2006, **133**, 137–156.
- 5 J.-C. Loison, V. Wakelam, K. M. Hickson, A. Bergeat and R. Mereau, *Mon. Notices Royal Astron. Soc.*, 2014, **437**, 930–945.
- 6 T. J. Millar and E. Herbst, *A&A*, 1994, **288**, 561–571.
- 7 R. J. Hargreaves, K. Hinkle and P. F. Bernath, *Mon. Notices Royal Astron. Soc.*, 2014, **444**, 3721.
- 8 M. Agúndez, J. Cernicharo, G. Quintana-Lacaci, A. Castro-Carrizo, L. Velilla Prieto, N. Marcelino, M. Guélin, C. Joblin, J. A. Martín-Gago, C. A. Gottlieb, N. A. Patel and M. C. McCarthy, *A&A*, 2017, **601**, A4.
- 9 NIST Standard Reference Database Number 101, <http://cccbdb.nist.gov/>, Release 16a edn, 2003.
- 10 J. N. Murrell, S. Carter, S. C. Farantos, P. Huxley and A. J. C. Varandas, *Molecular Potential Energy Functions*, John Wiley & Sons, Chichester, 1984.
- 11 M. Agúndez and V. Wakelam, *Chem. Rev.*, 2013, **113**, 8710–8737.
- 12 S. Yamamoto, S. Saito, M. Ohishi, H. Suzuki, S.-I. Ishikawa, N. Kaifu and A. Murakami, *ApJ*, 1987, **322**, L55–L58.
- 13 P. Thaddeus, C. A. Gottlieb, A. Hjalmarson, L. E. B. Johansson, W. M. Irvine, P. Friberg and R. A. Linke, *ApJ*, 1985, **294**, L49–L53.
- 14 J.-C. Loison, M. Agúndez, V. Wakelam, E. Roueff, P. Gratier, N. Marcelino, D. N. Reyes, J. Cernicharo and M. Gerin, *Mon. Notices Royal Astron. Soc.*, 2017, **470**, 4075–4088.

- 15 K. M. Hickson, J.-C. Loison and V. Wakelam, *Chem. Phys. Lett.*, 2016, **659**, 70–75.
- 16 D. C. Clary, E. Buonomo, I. R. Sims, I. W. M. Smith, W. D. Geppert, C. Naulin, M. Costes, L. Cartechini and P. Casavecchia, *J. Phys. Chem. A*, 2002, **106**, 5541–5552.
- 17 R. I. Kaiser, C. Ochsenfeld, M. Head-Gordon, Y. T. Lee and A. G. Suits, *Science*, 1996, **274**, 1508–1511.
- 18 T. Furtenbacher, I. Szabó, A. G. Császár, P. F. Bernath, S. N. Yurchenko and J. Tennyson, *ApJS*, 2016, **224**, 44–58.
- 19 A. G. G. M. Tielens, *Annu. Rev. Astron. Astrophys.*, 2008, **46**, 289–337.
- 20 C. A. Gottlieb, J. M. Vrtilek, E. W. Gottlieb, P. Thaddeus and A. Hjalmarson, *ApJ*, 1985, **294**, L55–L58.
- 21 S. Yamamoto, S. Saito, H. Suzuki, S. Deguchi, N. Kaifu, S.-I. Ishikawa and M. Ohishi, *ApJ*, 1990, **348**, 363–369.
- 22 M. Kanada, S. Yamamoto, S. Saito and Y. Osamura, *J. Phys. Chem.*, 1996, **104**, 2192–2201.
- 23 M. Caris, T. Giesen, C. Duan, H. Muller, S. Schlemmer and K. Yamada, *J. Mol. Spectrosc.*, 2009, **253**, 99–105.
- 24 M. C. McCarthy, K. N. Crabtree, M.-A. Martin-Drumel, O. Martinez, B. A. McGuire and C. A. Gottlieb, *ApJS*, 2015, **217**, 10.
- 25 Q. Jiang, C. M. L. Rittby and W. R. M. Graham, *J. Chem. Phys.*, 1993, **99**, 3194–3199.
- 26 S. M. Sheehan, B. F. Parsons, J. Zhou, E. Garand, T. A. Yen, D. T. Moore and D. M. Neumark, *J. Chem. Phys.*, 2008, **128**, 034301.
- 27 S. Yamamoto and S. Saito, *J. Chem. Phys.*, 1994, **101**, 5484–5493.
- 28 H. Ding, T. Pino, F. Güthe and J. P. Maier, *J. Chem. Phys.*, 2001, **115**, 6913–6919.
- 29 H. Yamagishi, H. Taiko, S. Shimogawara, A. Murakami, T. Noro and K. Tanaka, *Chem. Phys. Lett.*, 1996, **250**, 165–170.
- 30 J. Takahashi and K. Yamashita, *J. Chem. Phys.*, 1996, **104**, 6613–6627.
- 31 K. Aoki, S. Ikuta and A. Murakami, *J. Mol. Struct. THEOCHEM*, 1996, **365**, 103–110.
- 32 C. Ochsenfeld, R. I. Kaiser, Y. T. Lee, A. G. Suits and M. Head-Gordon, *J. Chem. Phys.*, 1997, **106**, 4141–4151.
- 33 R. K. Chaudhuri, S. Majumder and K. F. Freed, *J. Chem. Phys.*, 2000, **112**, 9301–9309.
- 34 J. C. Sancho-García and A. J. Pérez-Jiménez, *J. Phys. B: At., Mol. Opt. Phys.*, 2002, **35**, 3689–3699.
- 35 Y. Wang, B. J. Braams and J. M. Bowman, *J. Phys. Chem. A*, 2007, **111**, 4056–4061.
- 36 J. F. Stanton, *Chem. Phys. Lett.*, 1995, **237**, 20–26.
- 37 J. C. Saeh and J. F. Stanton, *J. Chem. Phys.*, 1999, **111**, 8275–8285.
- 38 P. Halvick, *Chem. Phys.*, 2007, **340**, 79–84.
- 39 M. K. Bassett and R. C. Fortenberry, *J. Chem. Phys.*, 2017, **146**, 224303.
- 40 S. C. Bennedjai, D. Hammoutène and M. L. Senent, *ApJ*, 2019, **871**, 255.
- 41 M. Perić, M. Mladenović, K. Tomić and C. M. Marian, *J. Chem. Phys.*, 2003, **118**, 4444–4451.
- 42 A. M. Mebel and R. I. Kaiser, *Chem. Phys. Lett.*, 2002, **360**, 139–143.
- 43 T. H. Dunning, *J. Chem. Phys.*, 1989, **90**, 1007–1023.
- 44 R. A. Kendall, T. H. Dunning and R. J. Harrison, *J. Chem. Phys.*, 1992, **96**, 6796–6806.
- 45 A. J. C. Varandas, *J. Chem. Phys.*, 2013, **138**, 054120.
- 46 A. J. C. Varandas, *J. Chem. Phys.*, 2013, **138**, 134117.
- 47 A. J. C. Varandas, in *Reaction Rate Constant Computations: Theories and Applications*, ed. K. Han and T. Chu, The Royal Society of Chemistry, 2013, ch. 17, pp. 408–445.
- 48 P. J. Knowles, C. Hampel and H. Werner, *J. Chem. Phys.*, 1993, **99**, 5219–5227.
- 49 P. Piecuch, M. Włoch and A. J. C. Varandas, *Topics in the Theory Of Chemical and Physical Systems*, Dordrecht, 2007, pp. 63–121.
- 50 R. J. Bartlett and M. Musia&poll, *Rev. Mod. Phys.*, 2007, **79**, 291–352.
- 51 T. Helgaker, P. Jørgensen and J. Olsen, *Molecular Electronic-Structure Theory*, John Wiley & Sons, Chichester, 2000.
- 52 H. J. Werner, P. J. Knowles, G. Knizia, F. R. Manby and M. Schütz *et al.*, *MOLPRO, a package of ab initio programs, version 2010.1*, 2010, Cardiff, U.K., 2010, see: <http://www.molpro.net>.
- 53 A. J. C. Varandas, *Annu. Rev. Phys. Chem.*, 2018, **69**, 177–203.
- 54 F. N. N. Pansini, A. C. Neto and A. J. C. Varandas, *Theor. Chem. Acc.*, 2016, **135**, 261–267.
- 55 A. J. C. Varandas and F. N. N. Pansini, *J. Chem. Phys.*, 2014, **141**, 224113.
- 56 F. N. N. Pansini, A. C. Neto and A. J. C. Varandas, *Chem. Phys. Lett.*, 2015, **641**, 90–96.
- 57 A. J. C. Varandas, *J. Chem. Phys.*, 2007, **126**, 244105.
- 58 A. J. C. Varandas, *J. Phys. Chem. A*, 2010, **114**, 8505–8516.
- 59 A. J. C. Varandas, *J. Phys. Chem. A*, 2011, **115**, 2668.
- 60 C. M. R. Rocha and A. J. C. Varandas, *J. Phys. Chem. A*, 2019, **123**, 8154–8169.
- 61 S. Joseph and A. J. C. Varandas, *J. Phys. Chem. A*, 2010, **114**, 2655–2664.
- 62 C. M. R. Rocha and A. J. C. Varandas, *Chem. Phys. Lett.*, 2018, **700**, 36–43.
- 63 K. A. Gingerich, H. C. Finkbeiner and R. W. Schmude, *J. Am. Chem. Soc.*, 1994, **116**, 3884–3888.
- 64 R. S. Urdahl, Y. Bao and W. M. Jackson, *Chem. Phys. Lett.*, 1991, **178**, 425–428.
- 65 B. E. Sagan, *The Symmetric Group: Representations, Combinatorial Algorithms, and Symmetric Functions*, Springer, New York, 2nd edn, 2001.
- 66 T. J. Lee and P. R. Taylor, *Int. J. Quantum Chem.*, 1989, **36**, 199–207.
- 67 C. L. Janssen and I. Nielsen, *Chem. Phys. Lett.*, 1998, **290**, 423–430.
- 68 T. J. Lee, *Chem. Phys. Lett.*, 2003, **372**, 362–367.
- 69 J. W. Huang and W. R. M. Graham, *J. Chem. Phys.*, 1990, **93**, 1583–1596.
- 70 G. H. Peslherbe, H. Wang and W. L. Hase, *Monte Carlo Sampling for Classical Trajectory Simulations*, Wiley-Blackwell, 1999, ch. 6, pp. 171–201.

- 71 W. L. Hase, R. J. Duchovic, X. Hu, A. Komornik, K. F. Lim, D. H. Lu, G. H. Peslherbe, K. N. Swamy, S. R. V. Linde, A. J. C. Varandas, H. Wang and R. J. Wolf, *QCPE Bull.*, 1996, **16**, 43.
- 72 A. J. Dean and R. K. Hanson, *Int. J. Chem. Kinet.*, 1992, **24**, 517–532.
- 73 V. Wakelam, J.-C. Loison, E. Herbst, B. Pavone, A. Bergeat, K. Béroff, M. Chabot, A. Faure, D. Galli, W. D. Geppert, D. Gerlich, P. Gratier, N. Harada, K. M. Hickson, P. Honvault, S. J. Klippenstein, S. D. L. Picard, G. Nyman, M. Ruaud, S. Schlemmer, I. R. Sims, D. Talbi, J. Tennyson and R. Wester, *ApJS*, 2015, **217**, 20.
- 74 R. L. LeRoy, *J. Phys. Chem.*, 1969, **73**, 4338–4344.
- 75 J.-C. Loison, X. Hu, S. Han, K. M. Hickson, H. Guo and D. Xie, *Phys. Chem. Chem. Phys.*, 2014, **16**, 14212–14219.